UCLA

UCLA Previously Published Works

Title

Quantum Simulation of Spin Models with Trapped Ions

Permalink

https://escholarship.org/uc/item/2kp9x84m

Authors

Campbell, WC
Monroe, C
Edwards, EE
et al.

Publication Date

2023-12-10

Peer reviewed

Quantum Simulation of Spin Models with Trapped Ions

C. Monroe, W. C. Campbell, E. E. Edwards, R. Islam, D. Kafri, S. Korenblit, A. Lee, P. Richerme, C. Senko, and J. Smith

Joint Quantum Institute
University of Maryland Department of Physics
College Park, MD 20742, USA

Summary. — Laser-cooled and trapped atomic ions form an ideal standard for the simulation of interacting quantum spin models. Effective spins are represented by appropriate internal energy levels within each ion, and the spins can be measured with near-perfect efficiency using state-dependent fluorescence techniques. By applying optical fields that exert optical dipole forces on the ions, their Coulomb interaction can be modulated in ways that give rise to long-range and tunable spin-spin interactions that can be reconfigured by shaping the spectrum and pattern of the laser fields. Here we review the theory behind this system, recent experimental data on the adiabatic prepration of complex ground states and dynamical studies with small collections of ions, and speculate on the near future when the system becomes so complex that its behavior cannot be modeled with conventional computers.

PACS 03.67 – a.
PACS 37.10 – Ty.
PACS 75.25 – j.

Introduction

The advent of individual atomic control with external electromagnetic fields, both involving internal states through optical pumping and external states through laser cool-

ing and electromagnetic trapping, has proven to be an ideal playground for quantum physics. This brand of physics has been well represented by the Enrico Fermi Courses over the last 25 years: *Laser Manipulations of Atoms and Ions* (1991), *Bose-Einstein Condensation in Atomic Gases* (1998), *Experimental Quantum Computation and Information* (2001), *Ultracold Fermi Gases* (2006), *Atom Optics and Space Physics* (2006), and *Atom Interferometry* (2013). The current 2013 course, *Ion Traps for Tomorrow's Applications*, specializes to the use of trapped atomic and molecular ions as probes of individual quantum systems, with many applications directed towards quantum information science. This lecture describes how a collection of laser-cooled atomic ions can serve as a programmable quantum simulator. The techniques outlined here also form a realistic basis for the development of a universal scalable quantum computer [1, 2, 3].

Quantum simulation, first promoted by Richard Feynman [4], exploits a controlled quantum system in order to study and measure the characteristics of a quantum model that may not be tractable using conventional computational techniques. A quantum simulator can be thought of as a special purpose quantum computer, with a reduced set of quantum operators and gates that pertain to the particular problem under study. While large-scale and useful quantum computation may be far off, the simulation of quantum problems that are difficult or even impossible to solve is just around the corner [5].

Quantum information hardware is conventionally represented by quantum bits (qubits), or controlled two-level quantum systems. A collection of interacting qubits directly maps to interacting effective spin systems, and therefore the simulation of quantum spin models is an appropriate place to start. Here we describe the use of the most advanced qubit hardware, trapped atomic ions, as effective spins [6, 7]. Trapped ion qubits enjoy an extreme level of isolation from the environment, can be entangled through their local Coulomb interaction, and can be measured with near-perfect efficiency with the availability of cyclic optical transitions [8]. Below we describe the first experiments that implement crystals of trapped atomic ions for the quantum simulation of spin models [9, 10, 11, 12, 13, 14, 15, 16].

Trapped Ion Effective Spins: Initialization, Detection, and Interaction

We represent a collection of effective spins by a crystal of atomic ions, with two electronic energy levels within each ion behaving as each effective spin or quantum bit (qubit). In the experiments reported in this lecture, atomic ^{171}Yb$^+$ ions are stored in a linear radiofrequency (Paul) ion trap, and the spin levels are the $^2S_{1/2}$ ground state "clock" hyperfine states, labeled by $|\uparrow\rangle_z$ ($F = 1, m_F = 0$) and $|\downarrow\rangle_z$ ($F = 0, m_F = 0$) and separated by a frequency of $\omega_0/2\pi = 12.64281$ GHz [17].

The spins are initialized through an optical pumping process, where resonant radiation tuned to the $^2S_{1/2}$ ($F = 1$) $-\,^2P_{1/2}$ ($F' = 1$) transition at a wavelength around 369.5 nm quickly and efficiently pumps each spin to state $|\downarrow\rangle_z$ after several scattering events, resulting in a > 99.9% state purity of each spin in a few microseconds. Following the controlled interaction between the spins depending on the particular quantum simula-
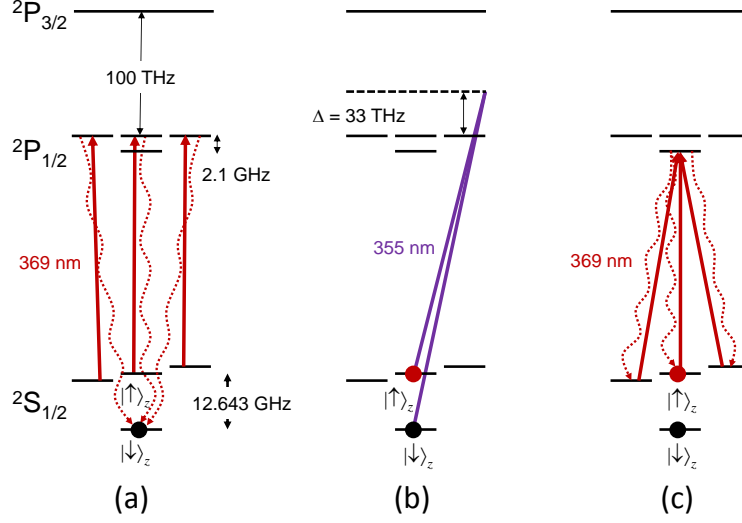
Fig. 1. – Relevant energy levels and couplings in the ^{171}Yb$^+$ atomic ion. The effective spin is stored in the $^2S_{1/2}$ $(F = 1, m_F = 0)$ and $(F = 0, m_F = 0)$ "clock" states, denoted by $|\uparrow\rangle_z$ and $|\downarrow\rangle_z$, respectively. The excited P states have a radiative linewidth of approximately 20 MHz. **(a)** Resonant radiation on the $^2S_{1/2}(F = 1) -^2 P_{1/2}(F' = 1)$ transition near 369 nm (solid lines) optically pumps each spin to the $|\downarrow\rangle_z$ state through spontaneous emission (wavy dotted lines). **(b)** Off-resonant radiation near 355 nm (solid lines) drives stimulated Raman transitions between the spin states, and by virtually coupling each spin to the collective motion of the ion chain, this coherent interaction underlies the spin-spin interaction as described in the text. **(c)** Resonant radiation on the $^2S_{1/2}(F = 1) -^2 P_{1/2}(F' = 0)$ transition near 369 nm (solid lines) causes the $|\uparrow\rangle_z$ state to fluoresce strongly (wavy dotted lines), while the $|\downarrow\rangle_z$ state is far from resonance and therefore dark. This allows the near-perfect detection of the spin state by the collection of this state-dependent fluorescence [17].

tion protocol described below, the spins are globally detected with laser radiation near resonant with the $^2S_{1/2}(F = 1) -^2 P_{1/2}(F' = 0)$ transition at a wavelength near 369.5 nm (Fig. 1). The effective detection efficiency of of each spin can be well above 99% [18]. This resonant optical interaction result in a small probability ($\sim 0.5\%$) of populating the metastable $^2D_{3/2}$ state upon spontaneous emission, and this atomic "leak" can be easily plugged with radiation coupling the $^2D_{3/2} -^3 D[3/2]_{1/2}$ transition at a wavelength near 935 nm [17]. In order to detect the spins in the σ_x or σ_y basis, previous to fluorescence measurement the spins are coherently rotated by polar angle $\pi/2$ along the y or x axis of the Bloch sphere.

Following the initialization of the spins but before their detection, spin-spin interactions can be implemented through off-resonant optical dipole forces [1, 19, 20, 21]. Conventionally, such forces are applied to subsets of ions in order to execute entangling quantum gates that are applicable to quantum information processing [8]. When such

forces are instead applied globally, the resulting interaction network allows the quantum simulation of a wide variety of spin models such as the Ising and Heisenberg spin chains [6, 7, 9, 10, 11, 12, 13, 14, 15, 16].

We uniformly address the ions with two off-resonant $\lambda \approx 355$ nm laser beams which drive stimulated Raman transitions [22, 23]. The beams intersect at right angles so that their wavevector difference Δk points along the direction of the ion motion perpendicular to the linear chain, which we denote by the X-direction Fig. 2. The effective interaction between the ions is therefore mediated by the collective transverse vibrations of the chain. We use the transverse modes of motion because their frequencies are tightly packed and all contribute to the effective Ising model, allowing control over the form and range of the interaction. Furthermore, the transverse modes are at higher frequencies, leading to better cooling and less sensitivity to external heating and noise[24].

In general, when noncopropagating laser beams have bichromatic beatnotes at frequencies $\omega_0 \pm \mu$, this can give rise to a spin-dependent force at frequency μ [6, 19]. Under the rotating wave approximation ($\omega_0 \gg \mu$) and within the Lamb-Dicke limit where $\Delta k \sqrt{\langle \hat{X}_i^2 \rangle} \ll 1$, with $\hat{X}_i$ the position operator of the ith ion, the resulting interaction Hamiltonian is [24]

$$(1) \qquad H(t) = \hbar \sum_i \Omega_i \Delta k \hat{X}_i \sigma_x^{(i)} \sin(\mu t).$$

Here, $\sigma_x^{(i)}$ is the Pauli spin flip operator on ion i with Rabi frequency Ω_i and $\Delta k \hat{X}_i = \sum_m \eta_{i,m}(a_m e^{-i\omega_m t} + a_m^\dagger e^{i\omega_m t})$ is written in terms of the normal mode phonon operators a_m and $a_m^\dagger$ at frequency ω_m. The Lamb-Dicke parameters $\eta_{i,m} = b_{i,m}\Delta k \sqrt{\hbar/2M\omega_m}$ include the normal mode transformation matrix $b_{i,m}$ of the ith ion with the mth normal mode, where $\sum_m |b_{i,m}|^2 = \sum_i |b_{i,m}|^2 = 1$ and M is the mass of a single ion.

The evolution operator under this Hamiltonian can be written as [25]

$$(2) \qquad U(\tau) = \exp\left[\sum_i \hat{\phi}_i \sigma_x^{(i)} + i \sum_{i,j} \chi_{i,j}(\tau)\sigma_x^{(i)}\sigma_x^{(j)} \right],$$

where $\hat{\phi}_i(\tau) = \sum_m [\alpha_{i,m}(\tau)a_m^\dagger - \alpha_{i,m}^*(\tau)a_m]$. The first term on the right hand side of Eq. (2) represents spin-dependent displacements of the mth motional modes through phase space by an amount

$$(3) \qquad \alpha_{i,m}(\tau) = \frac{-i\eta_{i,m}\Omega_i}{\mu^2 - \omega_m^2}[\mu - e^{i\omega_m\tau}(\mu\cos\mu\tau - i\omega_m\sin\mu\tau)].$$

The second term on the right hand side of Eq. (2) is a spin-spin interaction between ions

i and j with coupling strength

(4)
$$\chi_{i,j}(\tau) = \Omega_i \Omega_j \sum_m \frac{\eta_{i,m}\eta_{j,m}}{\mu^2 - \omega_m^2} \left[\frac{\mu\sin(\mu - \omega_m)\tau}{\mu - \omega_m} - \frac{\mu\sin(\mu + \omega_m)\tau}{\mu + \omega_m} + \frac{\omega_m\sin 2\mu\tau}{2\mu} - \omega_m\tau \right].$$

There are two regimes where multiple vibrational modes of motion contribute to the spin-spin coupling, taking evolution times τ to be much longer than the ion oscillation periods ($\omega_m\tau \gg 1$) [26]. In the "fast" regime, the optical beatnote detuning μ is close to one or more normal modes and the spins become entangled with the motion through the spin-dependent displacements. However, at certain times of the evolution $\alpha_{i,m}(\tau) \approx 0$ for all modes m and the motion nearly decouples from the spin states, which is useful for synchronous entangling quantum logic gates between the spins [27]. For the special case of $N = 2$ ions, both modes in a given direction decouple simultaneously when the detuning is set exactly half way between the modes, or at other discrete detunings, where both modes contribute to the effective spin-spin coupling. For larger numbers of ions, only the nearest few modes are coupled, and it is straightforward to calculate the appropriate duration and detuning for the gate. Faster pulses that couple to many or all modes may require more complex laser pulse shapes to suppress the residual entanglement to the phonon modes [25, 28].

In the "slow" regime, the optical beatnote frequency is far from each normal mode compared to that mode's sideband Rabi frequency ($|\mu - \omega_m| \gg |\eta_{i,m}\Omega_i|$). In this case, the phonons are only virtually excited as the displacements become negligible ($|\alpha_{i,m}| \ll 1$), and the result is a nearly pure Ising Hamiltonian from the last (secular) term of Eq. (4): $H_{eff} = \hbar \sum_{i,j} J_{i,j} \sigma_x^{(i)} \sigma_x^{(j)}$, where

(5)
$$J_{i,j} = \Omega_i \Omega_j \frac{\hbar(\Delta k)^2}{2M} \sum_m \frac{b_{i,m}b_{j,m}}{\mu^2 - \omega_m^2}.$$

For the remainder of this lecture, we consider interactions in this slow regime in order to engineer effective Hamiltonians that do not directly excite the normal modes of vibration.

Quantum Simulations of Magnetism

Quantum simulations of magnetism with trapped ions are of particular interest because the interaction graph can be tailored by controlling the external force on the ions, for instance by tuning the spectrum of lasers that provide the dipole force. This allows the control of the sign of the interaction from Eq. (5) (ferromagnetic vs. antiferromagnetic), the range, the dimensionality, and the level of frustration in the system. The effective spin-spin Hamiltonian originates from modulations of the Coulomb interaction and is therefore characterized by long-range coupling. The dynamics of the system can therefore become classically intractable for even modest numbers of spins $N > 30$.
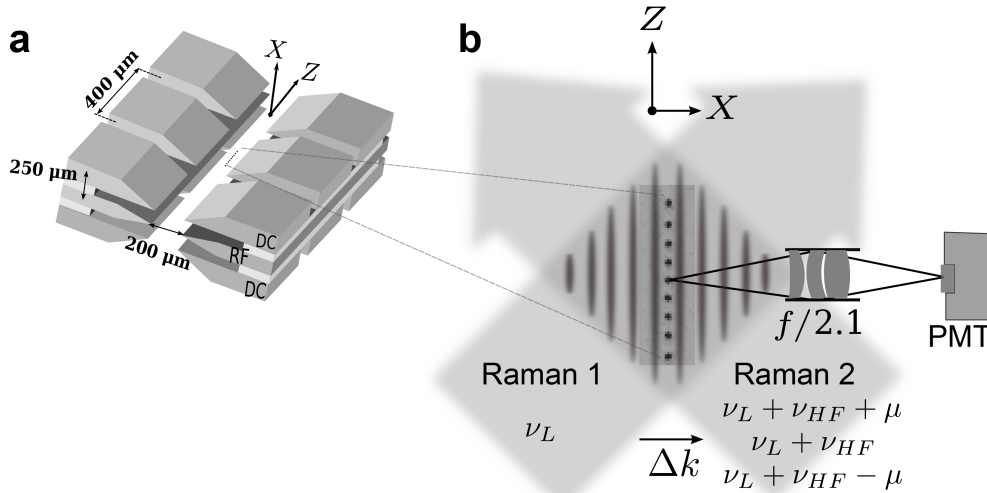
Fig. 2. – **(a)** Schematic of the three-layer linear radio frequency (Paul) trap, where the top and bottom layers carry static potentials and the middle one carries a radio frequency (rf) potential. **(b)** Two Raman beams globally address the ^{171}Yb$^+$ ion chain, with their wavevector difference (Δk) along the transverse (X) direction of motion, generating the Ising couplings through a spin-dependent force. The same beams generate an effective transverse magnetic field by driving resonant hyperfine transitions. A CCD image showing a string of nine ions (not in present experimental condition) is superimposed. A photomultiplier tube (PMT) is used to detect spin-dependent fluorescence from the ion crystal. (Reprinted from Ref. [12].)

We begin with the simplest nontrivial spin network, the Ising model with a transverse field. The system is described by the Hamiltonian

$$(6) \qquad H = \sum_{i<j} J_{i,j}\sigma_x^{(i)}\sigma_x^{(j)} + B_x \sum_i \sigma_x^{(i)} + B_y(t)\sum_i \sigma_y^{(i)},$$

where $J_{i,j}$ is given in Eq. (5) and is the strength of the Ising coupling between spins i and j, B_x is the longitudinal magnetic field, $B_y(t)$ is a time-dependent transverse field, and $\sigma_\alpha^{(i)}$ is the Pauli spin operator for the ith particle along the α direction. The couplings $J_{i,j}$ and field magnitudes B_x and $B_y(t)$ are given in units of angular frequency, with $\hbar = 1$.

For global addressing ($\Omega_i = \Omega$), the sum in Eq. (5) can be calculated exactly and we find that the Ising interactions are long-range and fall off approximately as $J_{i,j} \sim J/|i-j|^\alpha$. Even though the ions are not uniformly spaced and the couplings are somewhat inhomogeneous, this power-law approximation is a useful way to describe the physics of the simulated spin models. In the experiments, we realize a nearest-neighbor coupling $J \sim 2\pi \times 0.6$-0.7 kHz, and $0.5 < \alpha < 1.5$, although in principle the exponent can be tuned

from $0 < \alpha < 3$.

The effective transverse and longitudinal magnetic fields $B_y(t)$ and B_x in Eq. (6) drive Rabi oscillations between the spin states $|\downarrow\rangle_z$ and $|\uparrow\rangle_z$. Each effective field is generated by a pair of Raman laser beams with a beatnote frequency of ω_S, with the field amplitude determined by the beam intensities. The field directions are controlled through the beam phases relative to the average phase φ of the two sidebands which give rise to the $\sigma_x\sigma_x$ interaction in Eq. (6). In particular, an effective field phase offset of $0°$ ($90°$) relative to φ generates a σ_y (σ_x) interaction.

In principle, by controlling the spectrum of light that falls upon each ion in the linear chain, we can program arbitrary fully-connected Ising networks in any dimension [29]. In order to generate an arbitrary Ising coupling matrix $J_{i,j}$ it is necessary to have at least $N(N-1)/2$ independent controls. This can be accomplished by adding multiple spectral beatnote detunings to the Raman beams, and through individual ion addressing, varying the pattern of spectral component intensities directed to each ion. For simplicity, we consider the spectrum to contain N Raman beatnote detunings $\{\mu_n\}$ that are the same for all ions, where $n = 1, 2, ...N$. The coupling is therefore described by the $N \times N$ Rabi frequency matrix $\Omega_{i,n}$ of spectral component n at ion i. Note that the relative signs of the Rabi frequency matrix elements can be controlled by adjusting the phase of each spectral component. This individual spectral amplitude addressing provides N^2 control parameters, and the general Ising coupling matrix becomes

$$(7) \qquad J_{i,j} = \sum_{n=1}^{N} \Omega_{i,n}\Omega_{j,n} \sum_{m=1}^{N} \frac{\eta_{i,m}\eta_{j,m}\omega_m}{\mu_n^2 - \omega_m^2}$$

$$(8) \qquad \equiv \sum_{n=1}^{N} \Omega_{i,n}\Omega_{j,n}F_{i,j,n},$$

where $F_{i,j,n}$ characterizes the response of Ising coupling $J_{i,j}$ to spectral component n. An exact derivation of the effective Hamiltonian given a spectrum of spin-dependent forces gives rise to new off-resonant cross terms, which can be shown to be negligible in the rotating wave approximation, as long as the detunings are chosen so that their sums and differences do not directly encroach any sideband features in the motional spectrum of the crystal [24].

Given a desired Ising coupling matrix $J_{i,j}$, Eq. (8) can be inverted to find the corresponding Rabi frequency matrix $\Omega_{i,n}$. In order to simplify the problem, each beat note frequency can be tuned near a unique normal mode so that the response function $F_{i,j,n}$ has influence over all spins and modes. If we neglect the effect of each beatnode μ_n on modes with $n \neq m$, $F_{i,j,n}$ is separable in i and j and we can write $J_{i,j} = \sum_n R_{i,n}R_{j,n}$, or in matrix form, $\mathbf{J} = \mathbf{R}\mathbf{R}^{\mathrm{T}}$ where the matrix $R_{i,n} = \Omega_{i,n}\eta_{i,n}\sqrt{\frac{\omega_n}{\mu_n^2-\omega_n^2}}$. This quadratic equation can be inverted by diagonalizing the symmetric matrix $\mathbf{J}$ with some unitary matrix $\mathbf{U}$ so that $\mathbf{J}_{\mathrm{diag}} = \mathbf{U}\mathbf{J}$, then we simply write $\mathbf{R} = \mathbf{U}\sqrt{\mathbf{J}_{\mathrm{diag}}}$. As long as the eigenvalues of $\mathbf{J}$ are not too large, the matrix elements $R_{i,n}$ will be bounded. In practice
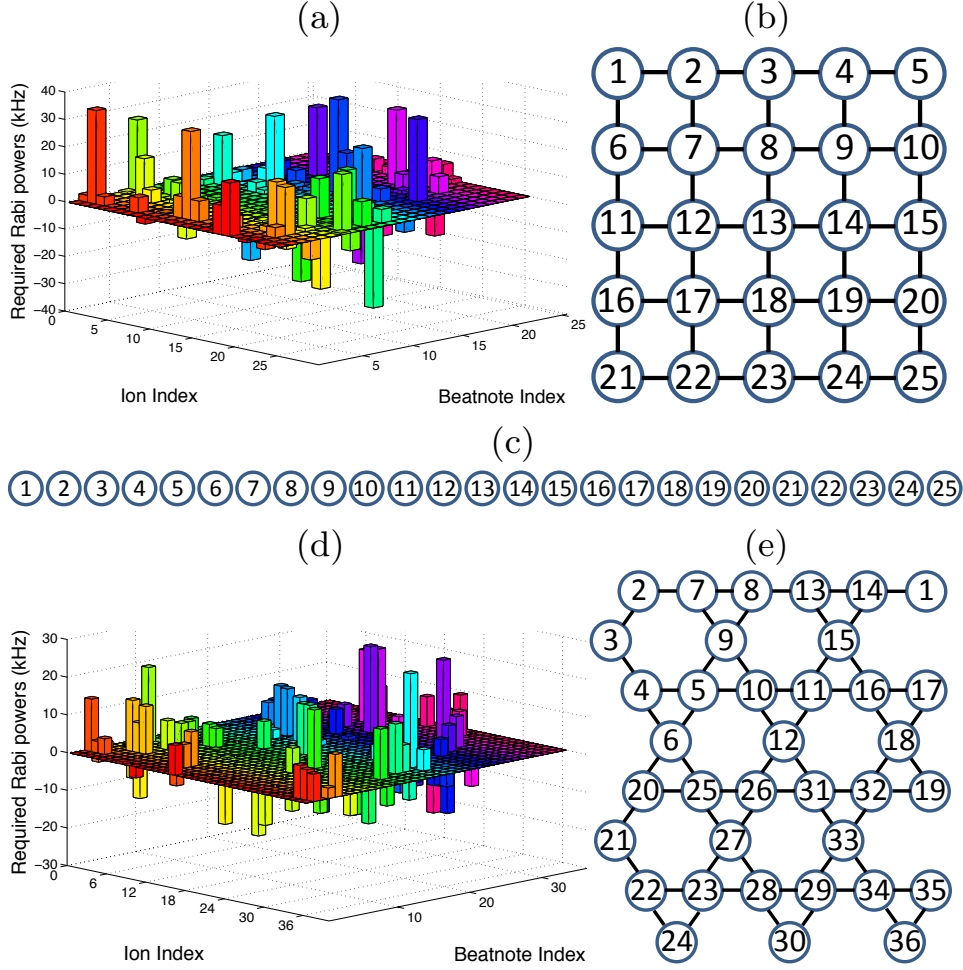
(a)

(b)

(c)

(d)

(e)

Fig. 3. – **(a)** Calculated Rabi frequency matrix $\Omega_{i,n}$ to generate the 2D square lattice shown in **(b)**, using a linear chain of $N = 25$ ions shown in **(c)**. The ion index refers to the order in the linear chain. **(d)** Calculated Rabi frequency matrix $\Omega_{i,n}$ to generate the 2D Kagomé lattice shown in **(e)** using a linear chain of $N = 36$ ions. In both cases the total optical power corresponds to a Rabi frequency of 10 MHz if focused on a single ion, the nearest-neighbor couplings are antiferromagnetic and we assume periodic boundary conditions over the unit cells shown. The ion index refers to the order in the linear chain. (Reprinted from Ref. [29].)

we can impose an upper bound on the total optical power (proportional to $\sum_{i,n} |\Omega_{i,n}|$) and implement numerical optimization techniques.

We now present two examples of solutions for $\Omega_{i,n}$ that produce interesting interaction graph topologies [29]. First we calculate a Rabi frequency matrix that results in a
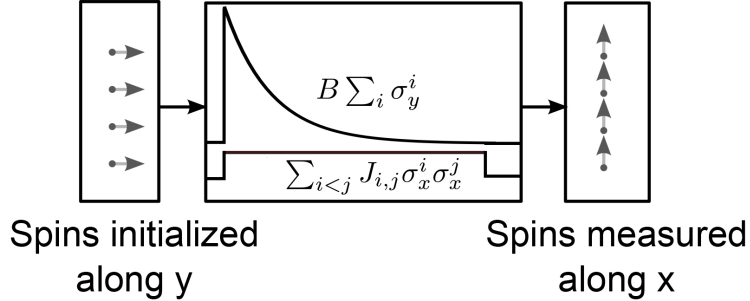
Fig. 4. – Adiabatic quantum simulation protocol in time (left to right). First, the spins are initially prepared in the ground state of $B_y \sum_i \sigma_y^i$, then the Hamiltonian 6 is turned on with starting field $B_y(0) \gg |J|$ followed by an exponential ramping to the final value B_y, keeping the Ising couplings $J_{i,j}$ fixed. Finally the $x-$ component of the spins is detected. (Reprinted from Ref. [12].)

nearest-neighbor 2D square antiferromagnetic lattice with $N = 25$ ions (5×5 grid with periodic boundary conditions), shown in Figs. 3(a) and (b). Next we produce a 2D Kagome lattice of antiferromagnetic interactions, a geometry that can support high levels of geometrical frustration [30], shown in Figs. 3c-d. In both cases we assume that the center-of-mass (COM) mode frequency is $\omega_1/2\pi = 5$ MHz, and the total optical power corresponds to a Rabi frequency of 10 MHz if focused on a single ion. The beatnote frequencies μ_m associated with mode m are each tuned blue of the mode m sideband by 10% of the spacing $\omega_1 - \omega_2$ between the most closely-spaced modes (the COM and "tilt" modes), which itself scales as $\log N/N^2$. In these examples, the sparse nearest-neighbor nature of the interaction graphs requires that most of the Ising interactions vanish, necessitating a high level of coherent control over all of the Ising couplings for this destructive interference.

Adiabatic Evolution and Preparation of the Ground State

Our experiments begin with the ions polarized along an effective magnetic field B_y transverse to long-range Ising couplings between the spins [9, 10]. The field is provided by global Raman carrier transitions on all ions. Once in an eigenstate (e.g., the ground state) of the transverse field, we experimentally ramp the field down, and given its final value, we then turn off the interactions and directly measure the state of each spin with a CCD camera, as depicted in the schematic of Fig. 4. If the field was ramped down adiabatically, we expect the resulting spin order to reflect the properties of the more interesting Ising couplings of the Hamiltonian.

Ferromagnetic order. – We realize effective ferromagnetic ground states by simply initially preparing the highest excited state of the coupled spin system, essentially flip-

ping the sign of the Hamiltonian. This is possible because there is little coupling to a thermal bath, and the effective spin temperature is zero. For such effective ferromagnetic couplings, we observe a clear phase transition from polarization along the transverse field (paramagnetic state) to ferromagnetic order, and recognize a sharpening in the transition point near the critical magnetic field as the number of spins is increased, as shown in Fig. 5 [12].

One order parameter is the average absolute magnetization (per site) along the Ising direction,

$$m_x = \frac{1}{N} \sum_{s=0}^{N} |N - 2s| P(s), \tag{9}$$

where $P(s)$ is the probability of having s spins along the Ising coupling direction. The Ising Hamiltonian in Eq. (6) has a global time reversal symmetry of $\{\sigma_x^i \rightarrow -\sigma_x^i, \sigma_z^i \rightarrow -\sigma_z^i, \sigma_y^i \rightarrow \sigma_y^i\}$ and this does not spontaneously break for a finite system, necessitating the use of average *absolute* value of the magnetization per site along the Ising direction as the relevant order parameter. For a large system, this parameter shows a second order phase transition, or a discontinuity in its derivative with respect to $B_y/|J|$. On the other hand, the fourth-order moment of the magnetization or Binder cumulant g [31, 32]

$$g = \frac{\sum_{s=0}^{N} (N - 2s)^4 P(s)}{\left(\sum_{s=0}^{N} (N - 2s)^2 P(s) \right)^2}, \tag{10}$$

becomes a step function at the QPT and should therefore be more sensitive to the phase transition. We illustrate this point by plotting the exact ground state order in the simple case of uniform Ising couplings for a moderately large system ($N = 100$) in Fig. 5(a). Here we scale the two order parameters to properly account for trivial finite size effects. The scaled magnetization and Binder cumulant are denoted by $\bar{m}_x$ and $\bar{g}$ respectively. In Fig 5(a) we also plot the exact ground-state order parameters for $N = 2$ and $N = 9$ spins. In Fig 5(b)-(d) we present data for these two order parameters as $B_y/|J|$ is varied in the adiabatic quantum simulation. Fig. 5(b) shows the scaled magnetization, $\bar{m}_x$ for $N = 2$ to $N = 9$ spins. The linear time scale indicates the exponential ramping profile of the (logarithmic) $B_y/|J|$ scale. Fig. 5(c) and (d) compare the two extreme system sizes in the experiment, $N = 2$ and $N = 9$ and clearly shows the increased steepness for larger system size. The scaled magnetization $\bar{m}_x$ is suppressed by $\sim 25\%$ in Figs. 5(b) and (c), and the scaled Binder cumulant $\bar{g}$ is suppressed by $\sim 10\%$ in Fig. 5(d) from unity at $B_y/|J| = 0$, predominantly due to decoherence from off-resonant spontaneous emission and additional dephasing due to intensity fluctuations in Raman beams during the simulation.

We compare the data shown in Fig. 5(c) and (d) to the theoretical evolution taking into account experimental imperfections and errors discussed below, including sponta-

neous emission to the spin states and to other states outside the target Hilbert space, and additional decoherence. The evolution is calculated by averaging $10,000$ quantum trajectories. This takes only one minute on a single computing node for $N = 2$ spins and approximately 7 hours, on a single node, for $N = 9$ spins. Extrapolating from this calculation suggests that averaging $10,000$ trajectories for $N = 15$ spins would require 24 hours on a 40 node cluster, indicating the inefficiency of classical computers to simulate even a small quantum system.

Antiferromagnetic order. – For antiferromagnetic simulations, we prepare the ground state of the transverse field and ramp the field down as before. However, in the antiferromagnetic case, the gaps are much smaller and the adiabaticity criterion is more stringent. Moreover, we must extract information on the spin positions, since the ground states are expected to exhibit staggered instead of uniform order. This information is provided by imaging the spins with an intensified CCD camera and recording the full configuration of all spins. Figure 6 shows the order seen following a ramp to zero field for $N = 10$ ions, where excited states are clearly created. Of the $2^{10} = 1024$ possible configurations, the two degenerate alternating-order ground states are produced about 18% of the time, with low-lying excitations also prevalent, as shown in the figure. Figure 7 shows similar data for $N = 14$ ions, with the resulting ground state population reduced to about 3% owing to the closing gap between ground and excited states. We also observe that as the interaction range is increased, the creation of excited states is more likely, since the increased level of frustration closes the gap even further and hinders adiabatic evolution. The magnetic-field ramp is controlled with a simple radiofrequency modulation source, and we can easily program any type of evolution in time. In addition to using standard exponential and linear ramps, we have also calculated the optimum ramp shape that maintains a constant adiabaticity parameter throughout the evolution, provided through prior knowledge of the many-body energy spectrum [14].

We have performed quantum simulations with up to $N = 18$ trapped ion spins. This system holds great promise for the quantum simluation of fully-connected spin chains with $50-100$ ions, where many aspects of the system such as dynamical processes become intractable.

By adding an axial field to an antiferromagnetic Ising Hamiltonian, we expect there to be many different orders to emerge as the axial field competes with the Ising couplings. We have been able to directly observe the steps between these orders by lowering the transverse field as before, but to a final state where only the Ising couplings and axial field remain. For N spins, we expect to see $[N/2]$ distinct phases in the ground state, owing to the long-range nature of the Ising interaction. Moreover, as N grows to infinity, the "Devil's staircase" structure [33] in magnetization becomes a fractal that arises since every rational filling factor (of which there are infinitely many) is a ground state [15]. Figure 8 shows the emergent ground state as the final axial field value is varied from low to high fields, with $N = 10$ ions.
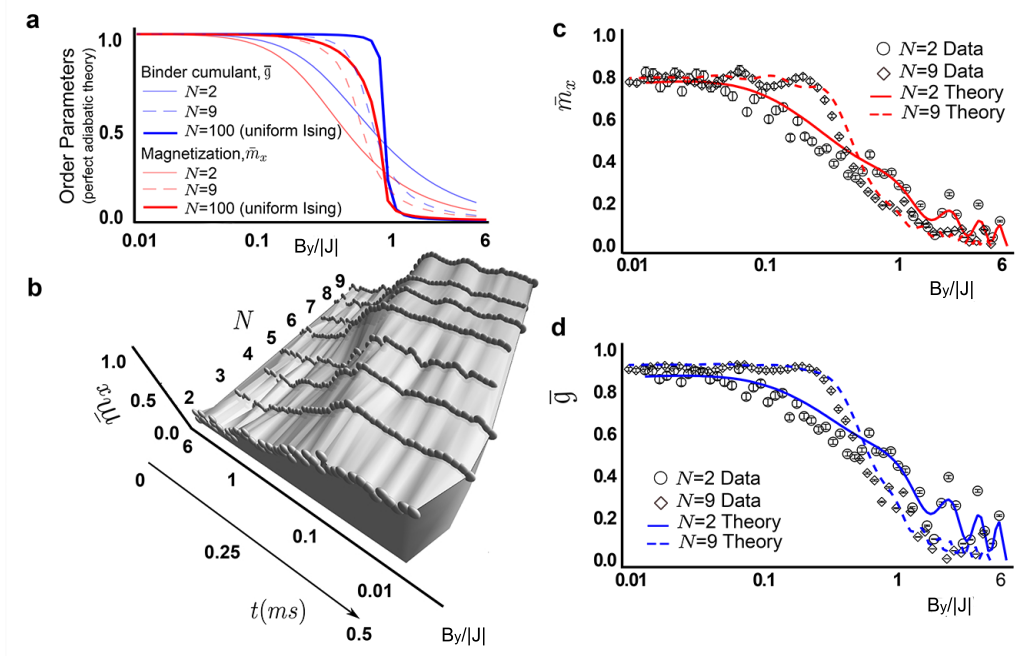
Fig. 5. – Observation of phase transition from paramagnetic phase $(B_y \gg |J|)$ to ferromagnetic order $(B_y \ll |J|)$ as transverse field is ramped down. **(a)** Theoretical values of order parameters $\bar{m}_x$ and $\bar{g}$ are plotted vs $B_y/|J|$ for $N = 2$ and $N = 9$ spins for ideal adiabatic time evolution. The order parameters are calculated by directly diagonalizing the Hamiltonian of Eq. (6). Order parameters are also calculated for a moderately large system $(N = 100)$ with uniform Ising couplings, to show the difference between the behaviors of $\bar{m}_x$ and $\bar{g}$. The scaled Binder cumulant $\bar{g}$ approaches a step function near the transition point $B_y/|J| = 1$ unlike the scaled magnetization $\bar{m}_x$, making it experimentally suitable to probe the transition point for relatively small systems. **(b)** Scaled magnetization, $\bar{m}_x$ vs $B_y/|J|$ (and simulation time) is plotted for $N = 2$ to $N = 9$ spins. As $B_y/|J|$ is lowered, the spins undergo a crossover from a paramagnetic to ferromagnetic phase. The crossover curves sharpen as the system size is increased from $N = 2$ to $N = 9$, prefacing a QPT in the limit of infinite system size. The oscillations in the data arise due to imperfect initial state preparation and non-adiabaticity due to finite ramping time. The (unphysical) 3D background is shown to guide eyes. **(c)** Magnetization data for $N = 2$ spins (circles) is contrasted with $N = 9$ spins (diamonds) with representative detection error bars. The data deviate from unity at $B_y/|J| = 0$ by $\sim 20\%$, predominantly due to decoherence from spontaneous emission in Raman transitions and additional dephasing from Raman beam intensity fluctuation, as discussed in the text. The theoretical time evolution curves (solid line for $N = 2$ and dashed line for $N = 9$ spins) are calculated by averaging over 10,000 quantum trajectories. **(d)** Scaled Binder cumulant $(\bar{g})$ data and time evolution theory curves are plotted for $N = 2$ and $N = 9$ spins. At $B_y/|J| = 0$ the data deviate by $\sim 10\%$ from unity, due to decoherence as mentioned before. (Reprinted from Ref. [12].)
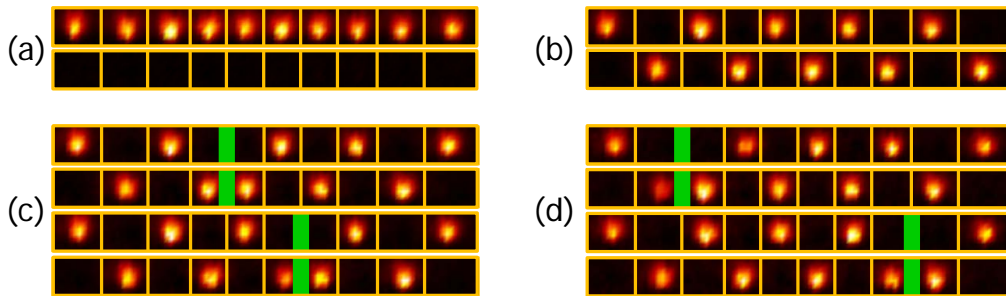
Fig. 6. – Magnetic ordering of $N = 10$ trapped atomic ion spins with long range antiferromagnetic Ising coupling, conveyed by the spatial images of the crystal having a length of 22μm. **(a)** Reference images of all spins prepared in state $|\uparrow\rangle_z$ (top) and $|\downarrow\rangle_z$ (bottom). **(b)** Ground-state staggered order of spins after adiabatically lowering the transverse magnetic field (measurements in the σ_x basis). These two degenerate states are produced a total of $\sim 18\%$ of the time. **(c)** Lowest (coupled) excited states, showing domain walls in green near the center of the crystal (measurements in the σ_x basis). Any of these four degenerate states are produced a total of $\sim 4\%$ of the time. **(d)** Next lowest (coupled) excited states, showing domain walls in green near the ends of the crystal (measurements in the σ_x basis), with these four degenerate states produced a total of $\sim 2\%$ of the time.

Quantum Dynamics and Quenches

As seen above, the adiabatic following of a many-body Hamiltonian requires a sufficiently large energy gap between the target state and the others states in the many body spectrum. For frustrated systems, this is generally a poor assumption and usually results in exponentially long ramp times to ensure adiabaticity. Here we now purposefully induce quantum dynamics in the system. The prediction of quantum dynamical processes in a many-body quantum system with long-range interactions is often more computationally difficult than the prediction of ground-state phases, and thus represents a new frontier of quantum simulations. Below we describe one of the first many-body quantum dynamical experiments, where a spin-spin interaction is suddenly switched on (a "quantum quench"). We are interested in the propagation of quantum correlations as they build up in space and time throughout the system.

For systems with only short-range interactions, Lieb and Robinson derived a constant-velocity bound that limits correlations to within a linear effective light cone [34]. In cold atomic systems such behavior was verified with quasiparticle short-range interactions in optical lattices [35]. However, for long-range quantum interactions, the speed with which correlations build up between distant particles is no longer guaranteed to obey the Lieb-Robinson prediction. In the case of strongly long-range interactions, for instance, the system behavior is highly non-local and can lead to effectively infinite propagation velocities. Breakdown of the Lieb-Robinson bound means that comparatively little can be predicted about the growth and propagation of correlations in long-range interacting systems, though there have been several recent theoretical and numerical advances [36,
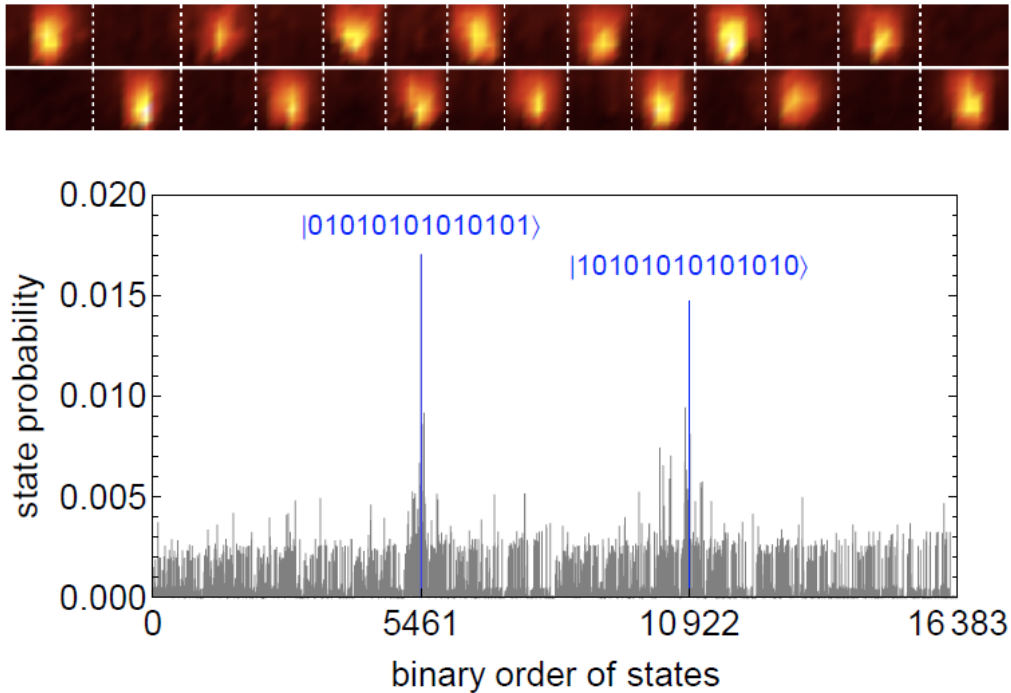
Fig. 7. – Distribution of configurations of $N = 14$ trapped atomic ion spins in the σ_x basis with long-range antiferromagnetic Ising couplings. The spins are initialized to be in the ground state in a strong effective magnetic field, and the field is ramped down to zero as the spins arrange according to the remaining Ising interactions. The top figures are images of the two expected ground states under the Ising couplings (measurements in the σ_x basis). The plot below is the measured probability of all $2^{14} = 16,384$ configurations, ranked by their binary index. The two ground states are most prevalent, with other states populated due to dynamics during the ramp.

37, 38, 39, 40, 41].

Here we report an experiment that directly measures the shape of the causal region and the speed at which correlations propagate within interacting spin chains [42]. To induce the spread of correlations, we perform a global quench by suddenly switching on the spin-spin couplings across the entire chain and allowing the system to coherently evolve. The dynamics following a global quench in a long-range interacting system can be highly non-intuitive; one picture is that of entangled quasi-particles at each site which propagate and interfere with one another, correlating distant parts of the system in a complicated way. This process differs substantially from local quenches, where a single site emits quasi-particles that travel ballistically [37, 43], resulting in a different causal region and propagation speed than in a global quench (even for the same spin model). A more detailed study of local quenches appears in Ref. [44].

In the experiments, we initialize a chain of 11 ions by optically pumping to the
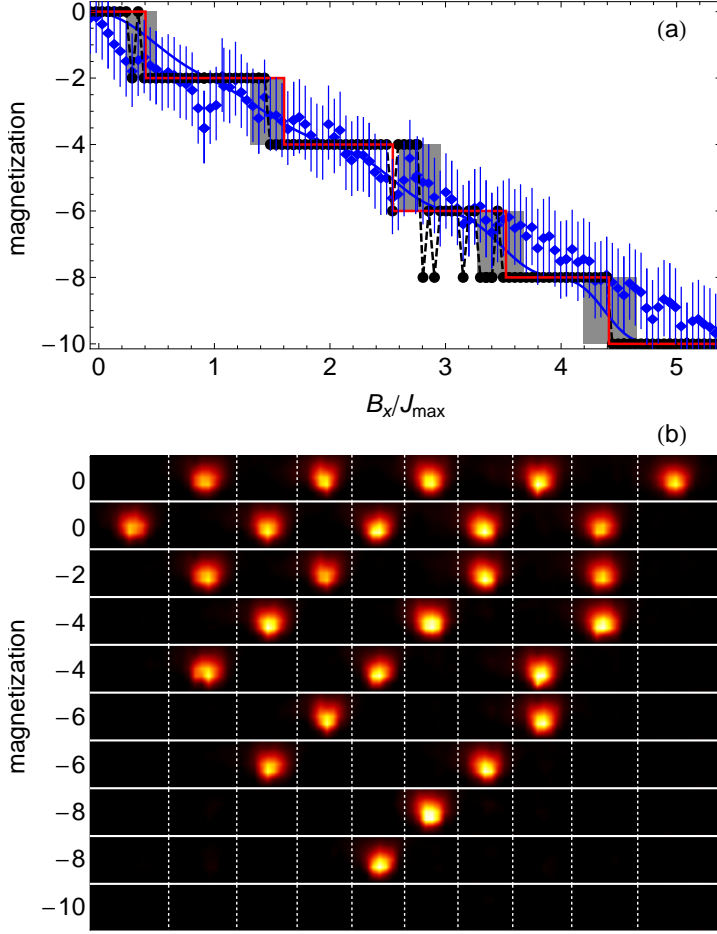
Fig. 8. – **(a)** Magnetization along the σ_x direction, in a chain of 10 ions for increasing axial field strength. The red, blue, and black curves correspond to the theoretical magnetization, average measured and simulated magnetization, and magnetization of the most probable state (respectively) for increasing B_x. Gray bands show the measurement uncertainty of the phase transition locations. **(b)** Linearly interpolated camera images of the ground-state spin configuration at each magnetization (measurements in the σ_x basis). (Reprinted from Ref. [15].)

product state $|\downarrow\downarrow\downarrow\ldots\rangle_z$. At $t = 0$, we quench the system by suddenly applying the Ising couplings at full strength, with the Ising couplings falling off with a particularly chosen power-law exponent α. We then allow coherent evolution for various lengths of time before measuring the spin state of each ion. The experiments at each time step are repeated 4000 times to collect statistics. To observe the buildup of correlations, we use the measured spin states to construct the connected correlation function $C_{i,j}(t)$ defined

as

$$(11) \qquad C_{i,j}(t) = \langle \sigma_i^z(t) \sigma_j^z(t) \rangle - \langle \sigma_i^z(t) \rangle \langle \sigma_j^z(t) \rangle,$$

between any pair of ions i and j at any time t. Since the system is initially in a product state, $C_{i,j}(0) = 0$ everywhere. As the system evolves away from a product state, evaluating Eq. (11) at all points in space and time provides the shape of the light-cone boundary and the correlation propagation velocity for our long-range spin models. We vary the interaction range over the values of the power-law exponent $\alpha = \{0.63, 0.83, 1.00, 1.19\}$ for these experiments, with the space-time correlations shown in Fig. 9. For values $\alpha < 1$, the system is strongly long-range, power law interactions are no longer reproducing, and even the generalized Lieb-Robinson bound [38] breaks down.
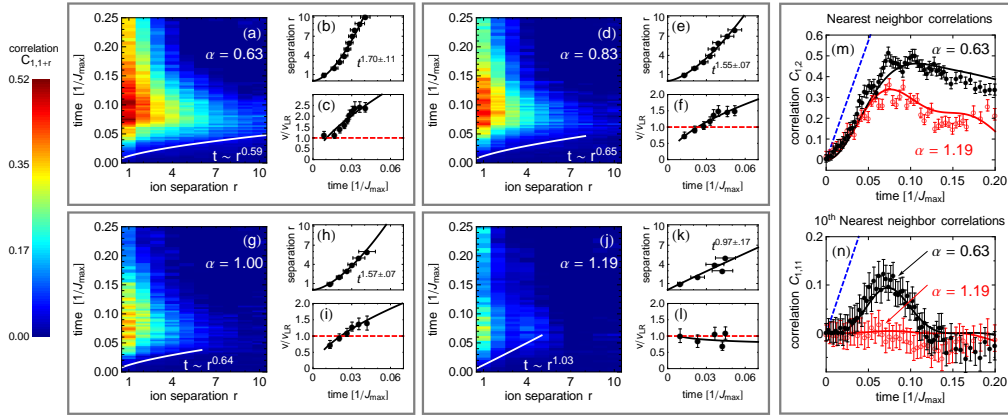

Fig. 9. – Spatial and time-dependent correlations **(a)**, extracted light-cone boundary **(b)**, and correlation propagation velocity **(c)** following a global quench of a long-range Ising model with $\alpha = 0.63$. The curvature of the boundary shows an increasing propagation velocity **(b)**, violating the constant-velocity Lieb-Robinson prediction v_{LR} **(c)**. Solid lines give a power-law fit to the data. Complementary plots are shown for $\alpha = 0.83$ **(d-f)**, $\alpha = 1.00$ **(g-i)**, and $\alpha = 1.19$ **(j-l)**. As the interaction range is made shorter, correlations do not propagate as far or as quickly through the chain, and the Lieb-Robinson velocity is followed. **(m,n)** Nearest- and 10th-nearest neighbor correlations for our shortest- and longest-range interaction compared to the exact solution (solid). The dashed blue curves show a generalized long-range bound for commuting Hamiltonians [41] (Reprinted from Ref. [42].)

In the limit of large transverse magnetic field $B_y \gg J$, processes in the $\sigma_i^x \sigma_j^x$ coupling which flip two spins (e.g. $\sigma_y^+ \sigma_y^+$) are energetically forbidden, leaving only the energy conserving flip-flop terms ($\sigma_y^+ \sigma_y^- + \sigma_y^- \sigma_y^+$). At times $t = 1/B$, the dynamics of the transverse field rephase and leave only a pure "XY" Hamiltonian

$$(12) \qquad H_{\mathrm{XY}} = \frac{1}{2} \sum_{i<j} J_{i,j} (\sigma_i^x \sigma_j^x + \sigma_i^z \sigma_j^z).$$

In the limit $B_y > |\eta_{i,m}\Omega_i|$, phonon contributions from the large transverse field can lead to unwanted spin-motion entanglement at the end of an experiment. Therefore, this method of generating an XY model requires the hierarchy $J \ll B \ll \eta\Omega$ for all spins i and modes m. For our typical trap parameters, $J/2\pi \approx 400$ Hz, $B/2\pi \approx 4$ kHz, and $|\eta_{i,m}\Omega/2\pi| \approx 20$ kHz.

We repeat the quench experiments for an XY model Hamiltonian using the same set of interaction ranges α, as shown in Fig. 10. Dynamical evolution and the spread of correlations in long-range interacting XY models are much more complex than in the Ising case since the Hamiltonian no longer commutes with itself. As a result, no exact analytic solution exists for the XY model.

Compared with the correlations observed for the Ising Hamiltonian, correlations in the XY model are much stronger at longer distances – particularly for short-range interactions. The multi-hop processes which were disallowed in the commuting Ising Hamiltonian now play a critical role in connecting distant spins. These processes also explain our observation of a steeper power-law scaling of the light-cone boundary in the XY model. However, we note that without an exact solution, there is no *a priori* reason to assume a power-law light-cone edge (used for the fits in Fig. 10), and deviations from power-law behavior might reveal themselves for larger system sizes.

An important observation in Fig. 10(j)-(l) is that of faster-than-linear light-cone growth for the relatively short-range interaction $\alpha = 1.19$. Although faster-than-linear growth is expected for $\alpha < 1$ (see previous section) and forbidden for $\alpha > 2$ [37, 41], no theoretical description of the light-cone shape exists in the intermediate regime $1 < \alpha < 2$. Our experimental observation has prompted us to numerically check the light-cone shape for $\alpha = 1.19$; we find that faster-than-linear scaling persists in systems of up to 22 spins before our calculations break down. Whether such scaling continues beyond ~ 30 spins is a question that at present only quantum simulators can hope to answer.

Outlook

While useful quantum computation may be years or even decades away, a restricted type of quantum computer with reduced connectivity will likely allow the simulation of quantum models that cannot be solved using classical computational methods. Such a quantum simulator will likely involve engineered interactions between qubits that may have a high degree of symmetry or involve certain global interactions. Trapped atomic ions are poised to become the platform for such demonstrations, with existing methods for engineering many-body quantum interactions whose graph is engineered through the use of external state-dependent dipole forces. Current experiments outlined in this lecture represent the state-of-the-art in the quantum simulation of spin models such as the transverse Ising and XY models, with up to ~ 20 interacting spins stored in trapped ions.

Soon, the trapped-ion platform may approach the level of $50 - 100$ interacting spins, where certain many-body phenomena cannot be modelled using classical physics or conventional computation. In this realm, it will become critical to verify and validate the
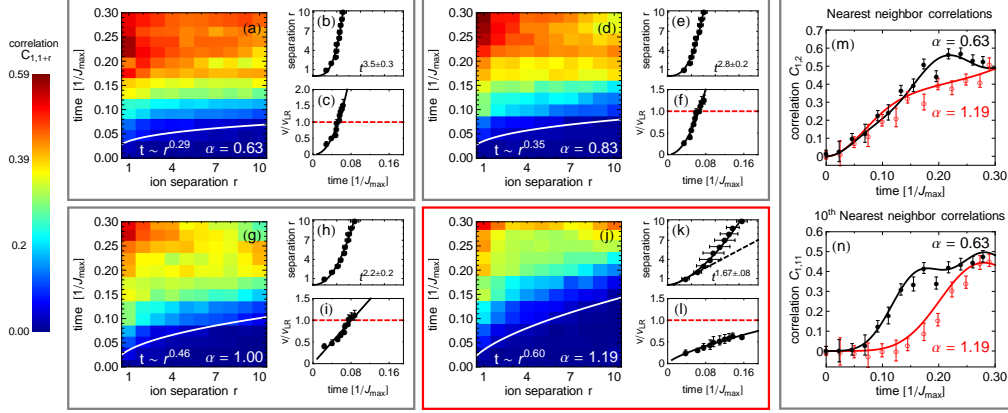
Fig. 10. – Global quench of a long-range XY model for four interaction ranges. **(a-l)**: Panel descriptions match those in Fig. 9. In each case when compared with the Ising model, correlations between distant sites in the XY model are stronger and build up more quickly. For the shortest-range interaction (**(j-l)**), we observe a faster-than-linear growth of the light-cone boundary, despite $\alpha > 1$; no analytic theory predicts this effect. **(m,n)** Nearest- and 10th-nearest neightbor correlations compared to a solution found by numerically evolving the Schrödinger equation of an exact XY model with experimental spin-spin couplings. (Reprinted from Ref. [42].)

quantum simulator [5]. To this end, it may be useful to exploit some degree of re-configurability of the spin system in order to test special (easy) cases of the target spin model, and the versitility of the trapped-ion system may prove useful for such an indirect verification of the simulator.

In the long run, scaling such ion trap systems to thousands or even larger numbers of qubits, for applications beyond quantum simulation will likely require some type of modular architecture. This may be afforded through the shuttling of ions between modules and through advanced trap structures [2] or the propagation of quantum information beween modules through photonic channels [3]. This ambitious venture will combine the current efforts in quantum simulation with many other techniques represented in this volume, in order to fulfill the ultimate ion trap application of tomorrow: universal quantum computation.

References

REFERENCES

[1] CIRAC J. I. and ZOLLER P., *Phys. Rev. Lett.*, **74** (1995) 4091.
[2] KIELPINSKI D., MONROE C. and WINELAND D., *Nature*, **417** (2002) 709.

[3] Monroe C., Raussendorf R., Ruthven A., Brown K. R., Maunz P., Duan L.-M. and Kim J., *Phys. Rev. A*, **89** (2012) 022317.

[4] Feynman R., *Int. J. Theor. Phys.*, **21** (1982) 467.

[5] *Nature Physics, Insight Issue: "Quantum Simulation,"*, **8** (2012) 264.

[6] Porras D. and Cirac J. I., *Phys. Rev. Lett.*, **92** (2004) 207901.

[7] Deng X.-L., Porras D. and Cirac J. I., *Phys. Rev. A*, **72** (2005) .

[8] Wineland D. and Blatt R., *Nature*, **453** (2008) 1008.

[9] Friedenauer A., Schmitz H., Glueckert J. T., Porras D. and Schaetz T., *Nature Physics*, **4** (2008) 757.

[10] Kim K., Chang M.-S., Islam R., Korenblit S., Duan L.-M. and Monroe C., *Phys. Rev. Lett.*, **103** (2009) 120502.

[11] Kim K., Chang M.-S., Korenblit S., Islam R., Edwards E. E., Freericks J. K., Lin G.-D., Duan L.-M. and Monroe C., *Nature*, **465** (2010) 590.

[12] Islam R., Edwards E., Kim K., Korenblit S., Noh C., Carmichael H., Lin G.-D., Duan L.-M., Wang C.-C. J., Freericks J. and Monroe C., *Nature Communications*, **2:377** (2011) .

[13] Edwards E. E., Korenblit S., Kim K., Islam R., Chang M.-S., Freericks J. K., Lin G.-D., Duan L.-M. and Monroe C., *Phys. Rev. B*, **82** (2010) 060412.

[14] Richerme P., Senko C., Smith J., Lee A., Korenblit S. and Monroe C., *Phys. Rev. A*, **88** (2013) 012334.

[15] Richerme P., Senko C., Korenblit S., Smith J., Lee A., Islam R., Campbell W. C. and Monroe C., *Phys. Rev. Lett.*, **111** (2013) 100506.

[16] Islam R., Senko C., Campbell W. C., S. K., Smith J., Lee A., Edwards E. E., Wang C.-C. J., Freericks J. K. and Monroe C., *Science*, **340** (2013) 583.

[17] Olmschenk S., Younge K. C., Moehring D. L., Matsukevich D. N., Maunz P. and Monroe C., *Phys. Rev. A*, **76** (2007) 052314.

[18] Noek R., Vrijsen G., Gaultney D., Mount E., Kim T., Maunz P. and Kim J., *Opt. Lett.*, **38** (2013) 4735.

[19] Mølmer K. and Sørensen A., *Phys. Rev. Lett.*, **82** (1999) 1835.

[20] Milburn G. J., Schneider S. and James D. F. V., *Fortschr. Phys.*, **48** (2000) 801.

[21] Solano E., de Matos Filho R. L. and Zagury N., *Phys. Rev. A*, **59** (1999) 2539(R).

[22] Hayes D., Matsukevich D. N., Maunz P., Hucul D., Quraishi Q., Olmschenk S., Campbell W., Mizrahi J., Senko C. and Monroe C., *Phys. Rev. Lett.*, **104** (2010) 140501.

[23] Campbell W. C., Mizrahi J., Quraishi Q., Senko C., Hayes D., Hucul D., Matsukevich D. N., Maunz P. and Monroe C., *Phys. Rev. Lett.*, **105** (2010) 090502.

[24] Zhu S.-L., Monroe C. and Duan L.-M., *Phys. Rev. Lett.*, **97** (2006) 050505.

[25] Zhu S.-L., Monroe C. and Duan L.-M., *Europhys. Lett.*, **73** (2006) 485.

[26] Sørensen A. and Mølmer K., *Phys. Rev. A*, **62** (2000) 022311.

[27] Sørensen A. and Mølmer K., *Phys. Rev. A*, **62** (2000) 022311.

[28] Choi T., Debnath S., Manning T. A., Figgatt C., Gong Z.-X., Duan L.-M. and Monroe C., *Phys. Rev. Lett.*, **112** (2014) 190502.

[29] Korenblit S., Kafri D., Campbell W. C., Islam R., Edwards E. E., Gong Z.-X., Lin G.-D., Duan L.-M., Kim J., Kim K. and Monroe C., *New Journal of Physics*, **14** (2012) 095024.

[30] Moessner R. and Ramirez A. P., *Phys. Today*, **59** (2006) 24.

[31] Binder K., *Zeitschrift fr Physik B Condensed Matter*, **43** (1981) 119.

[32] Binder K., *Phys. Rev. Lett.*, **47** (1981) 693.

[33] Bak P. and Bruinsma R., *Phys. Rev. Lett.*, **49** (1982) 249.

[34] Lieb E. and Robinson D., *Commun. Math. Phys.*, **28** (1972) 251.

[35] CHENEAU M., BARMETTLER P., POLETTI D., ENDRES M., SCHAUSZ P., FUKUHARA T., CHRISTIAN C., BLOCH I., KOLLATH C. and KUHR S., *Nature (London)*, **481** (2012) 484.

[36] SCHACHENMAYER J., LANYON B., ROOS C. and DALEY A., *Phys. Rev. X*, **3** (2013) 031015.

[37] HAUKE P. and TAGLIACOZZO L., *Phys. Rev. Lett.*, **111** (2013) 207202.

[38] HASTINGS M. and KOMA T., *Commun. Math. Phys.*, **265** (2006) 781.

[39] VAN DEN WORM M., SAWYER B., BOLLINGER J. and KASTNER M., *New J. Phys.*, **15** (2013) 083007.

[40] EISERT J., VAN DEN WORM M., MANMANA S. and KASTNER M., *e-print*, (2013) 1309.2308.

[41] GONG Z.-X., FOSS-FEIG M., MICHALAKIS S. and GORSHKOV A. V., *Phys. Rev. Lett.*, **113** (2014) 030602.

[42] RICHERME P., GONG Z.-X., LEE A., SENKO C., SMITH J., FOSS-FEIG M., MICHALAKIS S., GORSHKOV A. V. and MONROE C., *Nature*, **511** (2014) 198.

[43] CALABRESE P. and CARDY J., *Phys. Rev. Lett.*, **96** (2006) 136801.

[44] JURCEVIC P., LANYON B. P., HAUKE P., HEMPEL C., ZOLLER P., BLATT R. and ROOS C. F., *Nature*, **511** (2014) 202.